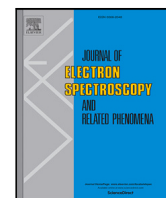


Ultrafast charge carrier dynamics in potassium-doped endohedral metallofullerene Sc₃N@C₈₀ thin films

Sebastian Emmerich, Sebastian Hedwig, Mirko Cinchetti, Benjamin Stadtmüller, Martin Aeschlimann

Angaben zur Veröffentlichung / Publication details:

Emmerich, Sebastian, Sebastian Hedwig, Mirko Cinchetti, Benjamin Stadtmüller, and Martin Aeschlimann. 2021. "Ultrafast charge carrier dynamics in potassium-doped endohedral metallofullerene Sc₃N@C₈₀ thin films." *Journal of Electron Spectroscopy and Related Phenomena* 252: 147110.
<https://doi.org/10.1016/j.elspec.2021.147110>.



Ultrafast charge carrier dynamics in potassium-doped endohedral metallofullerene $\text{Sc}_3\text{N}@C_{80}$ thin films

Sebastian Emmerich^{a,1}, Sebastian Hedwig^a, Mirko Cinchetti^b, Benjamin Stadtmüller^{a,*}, Martin Aeschlimann^a

^a University of Kaiserslautern and Research Center OPTIMAS, Erwin-Schrödinger-Straße 46, 67663 Kaiserslautern, Germany

^b Experimentelle Physik VI, Technische Universität Dortmund, 44221 Dortmund, Germany

ARTICLE INFO

Keywords:

Ultrafast exciton dynamics
Molecular thin films
Endohedral metallofullerene
Time- and angle-resolved photoelectron spectroscopy
Alkali metal doping

ABSTRACT

Molecular materials have emerged as highly flexible platform for photovoltaic and light-harvesting applications. One of the most important challenges for this class of materials is the trapping of charge carriers in bound electron–hole pairs, which severely limits the free charge carrier generation. Here, we demonstrate a significant modification of the exciton dynamics in thin films of endohedral metallofullerene complexes upon alkali metal doping. For the exemplary case of $\text{Sc}_3\text{N}@C_{80}$ thin films, we show that potassium doping results in an additional relaxation channel for the optically excited charge-transfer excitons that prevents the trapping of excitons in a long-lived Frenkel exciton-like state. Instead, potassium doping leads to an ultrafast exciton dissociation and most likely to the generation of free charge carriers. In this way, we propose alkali metal doping of molecular films as a novel approach to enhance the light-to-charge carrier conversion efficiency in photovoltaic molecular materials.

1. Introduction

One of the great promises of material science is to design and optimize materials for the next generation of high performance devices for different areas of application. This opportunity resulted in significant advances in the efficiency and the miniaturization of the active functional device units. Recently, similar efforts were devoted to consider more sustainable materials in device structures. In the field of light harvesting and photovoltaics, this would open a clear pathway towards the implementation of more sustainable energy sources that could convert solar power into charge and spin carriers with utmost efficiency [1].

In this regard, one of the most promising candidates for the active functional units in renewable and highly efficient photovoltaics applications are carbon-based molecular materials [2–5]. Their most intriguing feature is their chemical tunability, which allows one to design and control the most device-relevant properties by chemical synthesis on a molecular scale [6–10]. These properties are the energy position and the population dynamics of the most frontier molecular orbitals. They determine the absorption spectrum of the individual molecular units as well as the transport properties of electrons and holes within the molecular thin films and are responsible for the overall performance of

the molecular device structure. For this reason, many studies focused on the optical and electronic properties of thin films of highly tuneable molecular complexes and their derivatives on surfaces [6,7,11–21].

A very special and extremely tuneable family of molecular complexes are fullerenes [22]. The most famous fullerene is the buckminsterfullerene C_{60} [23]. Besides C_{60} , fullerenes can be synthesized with different numbers of atoms on the carbon cage or with incorporated atoms as well as small clusters of atoms inside the carbon cage, forming so called endohedral metallofullerenes (EMFs) [24–26]. Embedding spin-carrying metal centers into the carbon cage offers the opportunity to form single molecular magnets, or to manipulate the charge transport properties [6,20] as well as the excited state dynamics [21] of EMF films by the appropriate choice of the metallic centers inside the carbon cage.

In this work, we explore the tuneability of the ultrafast excited state dynamics of EMF materials. The excited state dynamics provide a direct view onto the microscopic mechanisms mediating or limiting the light-to-charge conversion efficiency in molecular materials. In contrast to metals or inorganic semiconductors, the optical excitation of molecular materials with visible light does not result in the formation of free carriers, but in bound electron–hole pairs, called excitons. These excitons

* Corresponding author.

E-mail address: bstadtmueller@physik.uni-kl.de (B. Stadtmüller).

¹ Present address: Division Mathematics for Vehicle Engineering MF, Fraunhofer Institute for Industrial Mathematics ITWM, Fraunhofer-Platz 1, 67663 Kaiserslautern, Germany.

can exhibit binding energies up to several hundred meV [27] and show different charge distributions as well as different degrees of spatial delocalization which are typically described in the limit of charge-transfer (CT) and Frenkel excitons. These different types of excitons can have long depopulation (decay) times up to several hundreds of microseconds [28–38]. In this context, the long depopulation times of the energetically lowest excitonic level as well as its large exciton binding energy severely limit the optically induced free carrier generation in molecular materials. This is one of the most severe challenges that must be tackled to improve the performance of molecular-based photovoltaic applications.

Therefore, we focus on the tunability of the exciton dynamics of EMF materials by potassium (K) doping. As exemplary case, we have selected the tri-metallic nitride fullerene $\text{Sc}_3\text{N}@C_{80}$ [24,25]. It consists of a very robust C_{80} carbon cage, which encapsulates three scandium (Sc) atoms coordinated to a central nitrogen (N) atom. This member of the EMF family is particularly interesting since its lowest unoccupied molecular orbital (LUMO) is not located at the carbon cage, but predominantly at the Sc_3N core [39]. This enables us not only to study the exciton dynamics at the carbon cage, but also to gain insights into potential cluster-cage charge transfer phenomena on ultrafast timescales.

In the following, we will show that K intercalation has a significant influence on the exciton dynamics of thin films of the prototypical endohedral metallofullerene $\text{Sc}_3\text{N}@C_{80}$. Using time- and angle-resolved photoemission with fs-XUV radiation, we find that the exciton dynamics of the pristine (undoped) molecular film are dominated by an exciton decay cascade starting with optically excited CT excitons and ending with a trapping of the excited carriers in a long-lived Frenkel-like excitonic state. Upon K doping, the decay cascade ends after the energetically lowest lying CT exciton which reveals a depopulation time smaller than 500 fs. This modification is caused by the dissociation of CT excitons due to their interaction with the partly ionized K atoms. We propose that this K-mediated dissociation of CT excitons very likely results in the generation of free charge carriers in homomolecular materials on ultrafast timescales.

2. Experimental details

2.1. Sample preparation

All experiments and sample preparation steps were performed under ultrahigh vacuum conditions with a base pressure better than 5×10^{-10} mbar. The Ag(111) single crystalline surface was prepared by repeated cycles of Ar⁺-sputtering and followed by annealing at $T_{\text{sample}} = 730\text{ K}$ for ≈ 40 min. The $\text{Sc}_3\text{N}@C_{80}$ molecules were evaporated onto the clean Ag(111) surface using a Knudsen type evaporation cell and an evaporation temperature of 790 K. The $\text{Sc}_3\text{N}@C_{80}$ multilayer films were prepared in several subsequent steps. First, a $\text{Sc}_3\text{N}@C_{80}$ monolayer film was prepared on the Ag(111) surface by thermal desorption of a multilayer film that was deposited beforehand onto the clean Ag(111) surface ($T_{\text{Desorb}} = 720\text{ K}$). The success of this sample preparation step was confirmed by the appearance of the characteristic diffraction pattern of a $\text{Sc}_3\text{N}@C_{80}$ monolayer film on Ag(111) [40]. Subsequently, $\text{Sc}_3\text{N}@C_{80}$ molecules were redeposited onto the $\text{Sc}_3\text{N}@C_{80}$ monolayer film. The molecular coverage was controlled by the evaporation time using a constant molecular flux of the Knudsen type evaporator. The coverage of the molecular thin film was estimated by the spectral lineshape and the intensity of valence band signatures of the $\text{Sc}_3\text{N}@C_{80}$ multilayer film in an angle-integrated photoemission spectroscopy experiment using the He- I_v emission line of a monochromatic He-discharge light source. The obtained valence band spectra of the $\text{Sc}_3\text{N}@C_{80}$ films are in very good agreement with previous photoemission data reported in literature [19,40]. The K doping was performed by dosing K atoms onto the $\text{Sc}_3\text{N}@C_{80}$ multilayer film at room temperature using a Saes Getters alkali metal dispenser. The K doping level x was estimated by the characteristic changes of the spectral lineshape of the $\text{Sc}_3\text{N}@C_{80}$ valence band structure which was reported earlier by Alvarez et al. [19].

2.2. Time- and angle-resolved photoelectron spectroscopy

The time- and angle-resolved photoelectron spectroscopy experiments were performed in an ultra-high vacuum photoemission chamber equipped with a hemispherical electron spectrometer (SPECS Phoibos 150), a high-precision six-axis manipulator and a fs-extreme ultraviolet (fs-XUV), 22.2 eV light source.

The fs-XUV radiation is obtained by high harmonic generation (HHG). A more detailed description of our setup can be found in Ref. [41]. Here, we only summarize the major parameters of our fs-XUV light source. It is based on a regenerative titanium sapphire chirped-pulse amplifier with sub-50 fs pulse duration, 10 kHz repetition rate and a pulse energy of 1 mJ at 780 nm wavelength. In our experiment, 90% of the beam intensity is used for generating the fs-XUV radiation. The fundamental radiation of the laser amplifier system is frequency-doubled in a β -barium borate (BBO) crystal and guided into a hollow waveguide that is filled with 30 torr of Kr gas. The HHG process itself takes place in the waveguide [42]. Using these conditions, the high harmonic spectrum exhibits a strong emission line at 22.2 eV (7th harmonic of the HHG spectrum), which is separated by 6.4 eV from the neighboring emission lines (5th and 9th harmonic of the HHG spectrum). The HHG radiation is linearly polarized and the orientation of the light polarization (p- or s- polarization with respect to the sample surface) can be adjusted by controlling the light polarization of laser radiation driving the HHG process. All experiments discussed in this article were performed with p-polarized fs-XUV radiation. After guiding the fs-XUV radiation to a set of transmissive Al and Sn filters, it is focused onto the sample surface using a toroidal mirror.

The remaining 10% of the primary beam intensity of the titanium sapphire amplifier (≈ 0.1 mJ) is available for the optical excitation of the molecular films. This part of the beam is frequency-doubled in a second BBO crystal (photon energy: 3.2 eV, spectral band width: 0.04 eV) and is focused on the sample surface. The polarization of the pump pulse is adjusted with a combination of a linear polarizer and a half-wave plate and is set to p-polarization for all experiments reported here. The time delay between the optical pump and the fs-XUV probe pulse is controlled by a delay stage operating with 1 μm longitudinal resolution. Prior to each experiment, the spatial and temporal overlap of the pump and probe pulses on the sample surface was carefully adjusted and checked regularly during the series of measurements. For each sample, we also characterized the influence of pump- or probe-induced space charge effects on the temporal and spectral shape of our time-resolved photoemission data. For all experiments discussed here, we checked regularly for radiation-induced degradation of the molecular thin films.

3. Results and discussion

3.1. Ultrafast exciton dynamics of a pristine $\text{Sc}_3\text{N}@C_{80}$ thin film

We start our discussion with the pristine $\text{Sc}_3\text{N}@C_{80}$ thin film ($\Theta_{\text{Sc}_3\text{N}@C_{80}} \approx 5\text{ ML}$). The exciton dynamics was investigated in real-time using time-resolved photoelectron spectroscopy with p-polarized fs-XUV radiation. Crucially, the large photon energy of the probe beam allows us to simultaneously monitor the excited state dynamics as well as the transient changes in the occupied valence levels of the entire molecular film. The latter reflects the collective response of the electron system to the optical excitation of non-interacting excitons within the molecular thin film. For instance, the formation of charge transfer (CT) excitons can lead to a transient inhomogeneous linewidth broadening of all molecular valence states which is absent for Frenkel excitons [34, 35]. Hence, the transient linewidth broadening of all molecular valence states is a clear spectroscopic signature of CT excitons in molecular materials.

The exciton dynamics of the $\text{Sc}_3\text{N}@C_{80}$ film is shown as a two-dimensional plot of the time-dependent photoemission intensity in Fig. 1(a). For the optical excitation, we used a laser fluence of

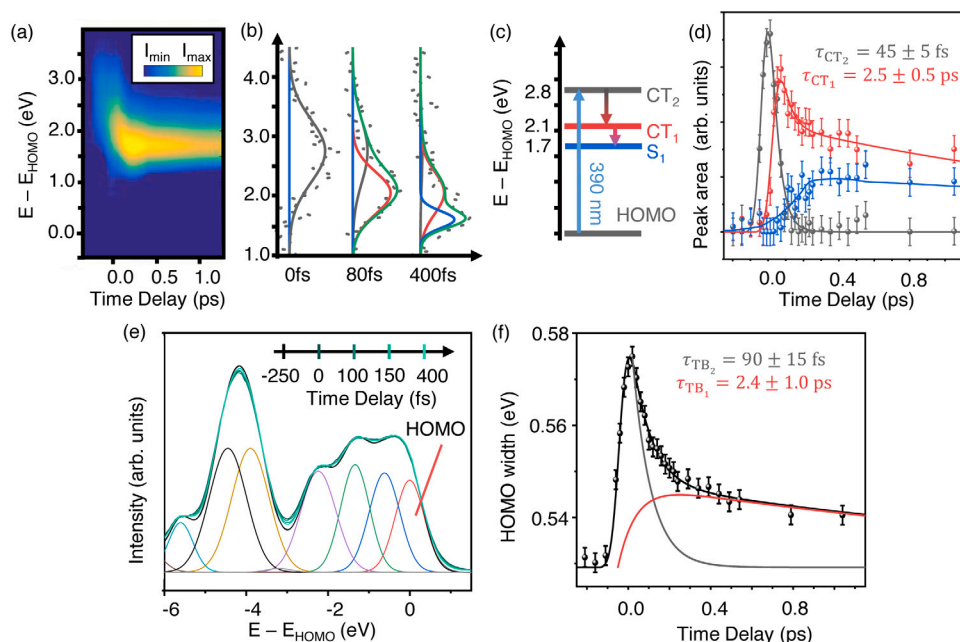


Fig. 1. Exciton dynamics of a pristine $\text{Sc}_3\text{N}@C_{80}$ multilayer film ($\theta \approx 5$ ML). (a) 2D map of the time-resolved photoemission yield of the excited states after optical excitation with fs 3.2 eV laser pulses ($F = 0.55 \frac{\text{mJ}}{\text{cm}^2}$). (b) Exemplary photoemission spectra of the excited state energy range at selected time delays. The Gaussian curves underneath the experimental data represent the fitting model employed to determine the spectral weight of the three excitonic levels CT_2 , CT_1 and S_1 that dominate the excited state dynamics of the $\text{Sc}_3\text{N}@C_{80}$ multilayer film. The envelope of the fitting model is superimposed onto the experimental data as green curve. (c) Experimentally determined energy level diagram of the excited states of the $\text{Sc}_3\text{N}@C_{80}$ multilayer film. (d) The population dynamics of the three excitonic levels shown in (b). (e) Valence band structure of the studied $\text{Sc}_3\text{N}@C_{80}$ film for different pump-probe time delays (shown in green colors). The colored Gaussian curves illustrate the fitting model employed for analyzing the transient lineshape of the valence band structure. (f) Transient change of the linewidth (FWHM) of the HOMO state (dots, red Gaussian in (e)). The temporal evolution of the FWHM is fitted with a double exponential decay function convoluted with the pump-probe cross-correlation curve (solid line).

$F = 0.55 \frac{\text{mJ}}{\text{cm}^2}$. This fluence F leads to exciton dynamics in the linear regime where the timescales of the exciton dynamics do not depend on the applied fluence and are hence sufficiently low to avoid nonlinear effects in the exciton dynamics [34,35].

The photoemission yield was recorded in normal emission geometry and averaged over a momentum range of $\pm 0.5 \text{ \AA}^{-1}$ around the $\bar{\Gamma}$ -point of the surface Brillouin zone. Exemplary photoemission spectra of the excited states are shown in Fig. 1(b) for three selected time steps. These characteristic changes in the spectra already allow us to identify the signatures of three excitonic states that contribute to the excited states of the $\text{Sc}_3\text{N}@C_{80}$ thin film. After optical excitation with 3.2 eV photons (p-polarized light), we find an instantaneous accumulation of spectral density 2.8 eV above the highest occupied molecular orbital (HOMO) of the $\text{Sc}_3\text{N}@C_{80}$ molecules. This photoemission signal is assigned to the CT_2 level, which is resonantly excited from the HOMO level of the molecular thin film despite the energy mismatch between the intrinsic excited state energy of the CT_2 exciton and the photon energy of the pump pulses. This is possible due to the extremely large linewidth of the HOMO and the CT_2 exciton level in conjunction with the spectral bandwidth of the ultrashort pump pulses. The transient population of the CT_2 state decays into a lower lying excitonic state (referred to as CT_1) before becoming trapped in the excited state S_1 with significantly smaller spectral linewidth (full width at half maximum, FWHM) and a depopulation time of $\tau_{\text{S}_1} \gg 1$ ps.

To quantify the energy level alignment of these three excitonic states, we employed a dedicated fitting model with three Gaussian curves to describe the time-dependent spectral density at each time step during the exciton decay cascade. This model is very similar to the three-Gaussian model that was recently applied to successfully capture the exciton dynamics of other fullerene thin films on noble metal surfaces [34,35]. For the $\text{Sc}_3\text{N}@C_{80}$ thin film, the best fitting quality was obtained with the three Gaussian curves shown underneath the experimental data (gray dots) in Fig. 1(b). The fitting envelope is included as green curve. The spectral features of the CT_2 , CT_1 and S_1

excitons are centered at $E_{\text{CT}_2} - E_{\text{HOMO}} = 2.8$ eV, $E_{\text{CT}_1} - E_{\text{HOMO}} = 2.1$ eV, and $E_{\text{S}_1} - E_{\text{HOMO}} = 1.7$ eV, respectively. These fitting results are summarized in the corresponding energy level diagram of the excited states in Fig. 1(c). Hence, our quantitative spectral analysis also confirms that (at least) three excitonic levels contribute to the excited state dynamics of the $\text{Sc}_3\text{N}@C_{80}$ thin films after optical excitation with blue light.

In a second step, we extracted the population dynamics of each excitonic state by constraining the excited state energy and the linewidth (FWHM) of each excited state to a fixed value. The only free fitting parameters are the peak intensities (areas) of the three Gaussian curves which are shown in Fig. 1(d) as colored dots. The solid lines of identical color represent the fitting model to determine the depopulation (decay) time of each excitonic state. The CT_2 exciton is formed instantaneously after the optical excitation (within our experimental uncertainty) and directly decays into the lower lying CT_1 exciton within $\tau_{\text{CT}_2} = 45 \pm 5$ fs (gray curve). The decay dynamics of CT_1 can only be described by a double-exponential decay (see red curve in Fig. 1(d)) with two significantly different depopulation times of $\tau_{\text{CT}_{1,1}} = 50 \pm 5$ fs and $\tau_{\text{CT}_{1,2}} = 2.5 \pm 1.0$ ps. Subsequently, the population of the S_1 exciton increases within the first 200 fs before staying almost constant for all times investigated in our experiment. This points to an excitonic lifetime of the S_1 level of $\tau_{\text{S}_1} \gg 10$ ps.

Note that the double-exponential decay trace of the CT_1 exciton is not caused by the existence of two distinct excitonic states in this excited state range which could not be separated in our data analysis procedure. It is rather the result of the limited data quality which did not allow us to model the continuously changing lineshape of the hot CT_2 exciton during its transformation into the CT_1 exciton. Hence, we propose that the true thermalization or depopulation time constant of the CT_2 exciton is reflected by the sum of τ_{CT_2} and $\tau_{\text{CT}_{1,1}}$ and amounts to ≈ 100 fs.

The ultrafast dynamics of the occupied valence band structure during the formation and decay cascade of the excitonic states is reflected in the momentum integrated photoemission spectra at selected time

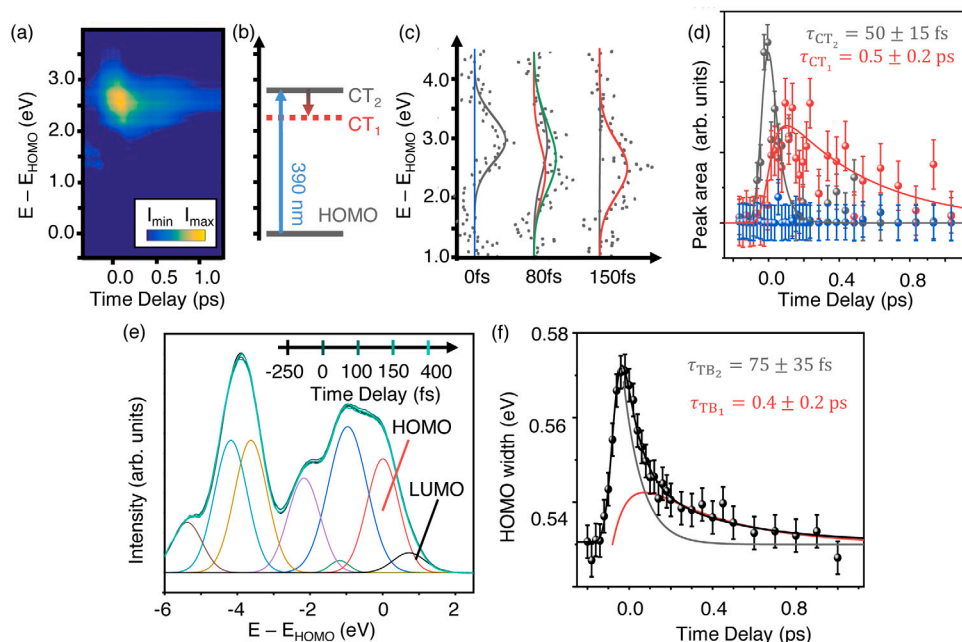


Fig. 2. Exciton dynamics of a K-doped $K_1(\text{Sc}_3\text{N}@C_{80})$ multilayer film. (a) 2D map of the time-resolved photoemission yield of the excited states after optical excitation with 3.2 eV laser pulses ($F = 0.55 \frac{\text{mJ}}{\text{cm}^2}$). The energy level diagram of the excited states is illustrated in (b), exemplary photoemission spectra of the excited state energy range at selected time delays are shown in (c). The Gaussian curves underneath the experimental data represent the fitting model employed to determine the spectral weight of the two excitonic levels CT_2 and CT_1 . The envelope of the fitting model is superimposed onto the experimental data as green curve. (d) Population dynamics of the three excitonic levels shown in (b). (e) Valence band structure of the studied K-doped $\text{Sc}_3\text{N}@C_{80}$ film for different pump-probe time delays (shown in green colors). The colored peaks illustrate the fitting model employed for analyzing the transient lineshape of the valence band structure. (f) Transient change of the linewidth (FWHM) of the HOMO state (dots, red Gaussian in (e)). The temporal evolution of the FWHM is fitted with a double-exponential decay function convoluted with the pump-probe cross-correlation curve (solid line).

delays in Fig. 1(e). These data were recorded simultaneously with the excited state photoemission data and are also averaged over a momentum range of $\pm 0.5 \text{ \AA}^{-1}$ around the \bar{F} -point of the surface Brillouin zone. The quasi-static lineshape of the valence band states of the $\text{Sc}_3\text{N}@C_{80}$ multilayer film is reflected in the energy distribution curve (EDC) recorded prior to the optical excitation. It consists of the spectroscopic signatures of the HOMO as well as the lower lying molecular orbitals (HOMO-X). The energy positions and relative linewidth of the valence band features matches perfectly with previous photoemission studies of $\text{Sc}_3\text{N}@C_{80}$ multilayer films on different surfaces [19,40].

Upon optical excitation and creation of excitons, the linewidth (FWHM) of all molecular features increases instantaneously (within our experimental resolution) before transforming back to their original state. The relaxation dynamics are clearly slower than the excitation dynamics and occur only within several hundreds of fs. This transient broadening of all molecular valence orbitals reflects the many-body response of the molecular material to the optically excited excitons. In the particular case of CT excitons, the spatial separation of electron and hole on neighboring molecular sites results, in first approximation, in an electric dipole within the highly polarizable molecular material. The dipolar field of the individual CT excitons causes a Stark-like shift of the energy levels of the surrounding molecules. The magnitude and sign of the energy shift depends strongly on the relative position between the molecule and the CT exciton. In total, these individual shifts add up to an inhomogeneous linewidth broadening of the molecular valence band structure of the fullerene thin films [34,35]. Hence, the transient broadening can be understood as the spectroscopic signature of CT excitons in the molecular material [34,35]. For our case study, the observation of the transient broadening of the $\text{Sc}_3\text{N}@C_{80}$ valence band structure points to the existence of CT excitons in the $\text{Sc}_3\text{N}@C_{80}$ film after the optical excitation.

The transient changes of the valence band structure were quantified by applying a dedicated fitting procedure. First, each spectrum of the time-resolved photoemission data was fitted individually using the fitting model shown underneath the experimental data in Fig. 1(e). This

model was adapted from Seidel et al. [40] and the energy positions as well as the areas of each peak were optimized for the photoemission spectrum at $\Delta t = -250$ fs. During the fitting routine, we constrained the relative energy position and the peak area of all Gaussian peaks. This is possible due to the extremely low strength of the optical excitation and the correspondingly marginal depopulation of the HOMO level that is insignificant in our experimental data. The only free parameters are the transient full width at half maximum (FWHM) of all Gaussian peaks of our fitting model.

The extracted transient evolution of the linewidth (FWHM) of the HOMO level is shown in Fig. 1(f) which reveals the identical temporal behavior as observed for all other molecular features of the $\text{Sc}_3\text{N}@C_{80}$ film. We find an instant rise of the transient linewidth after optical excitation within our fs temporal resolution [41] followed by a double-exponential decay with two significantly different time constants. These time constants are $\tau_{\text{TB}2} = 90 \pm 15$ fs and $\tau_{\text{TB}1} = 2.5 \pm 0.5$ ps with a maximum amplitude of the transient broadening of $\Delta\text{FWHM}_{\text{max,TB}2} = 45 \pm 2$ meV and $\Delta\text{FWHM}_{\text{max,TB}1} = 11 \pm 2$ meV. The extracted time constants of the transient broadening match almost perfectly to the depopulation times of the CT_2 and the CT_1 excitons, but not the one of the S_1 exciton. This close link between these time constants clearly shows that the transient broadening can indeed be attributed to the formation of CT excitons and that only the CT_2 and CT_1 excitons are CT excitons. Instead, S_1 is attributed to a Frenkel-like exciton with electron and hole located on the same molecular site. Interestingly, the magnitude of the transient broadening is significantly smaller compared to the metal-free fullerene C_{60} [34,35]. This observation can unfortunately not directly be correlated to a different charge distribution of the CT excitons in both molecular systems but might also be due to the different polarizability of both fullerene thin films [43].

Together, our findings for the exciton population dynamics (excited states) and the transient charge character of the excitons (valence states) provide a clear picture of the exciton dynamics in the pristine $\text{Sc}_3\text{N}@C_{80}$ film. Optical excitation with 3.2 eV photons results in the

instantaneous formation of hot excitons with at least partial CT character (referred to as CT_2). These CT_2 excitons thermalize within 100 fs and transform continuously into the CT_1 excitons with lower excited state energy. In a second step, the CT_1 excitons further decay into the S_1 excitons with dominant Frenkel exciton-like character where they become trapped for at least 10 ps. Interestingly, the energy of the S_1 exciton ($E - E_{HOMO} = 1.7$ eV) is still significantly larger than the energy of the LUMO-derived molecular state inside the carbon cage [19,40]. This suggests that the exciton dynamics of all three excitonic states CT_2 , CT_1 and S_1 only involves excited states that are located at the carbon cage, but not a LUMO-derived excitonic state at the $Sc_3N@C_{80}$ core. The exciton dynamics of the endohedral fullerene $Sc_3N@C_{80}$ is hence very similar to the exciton dynamics of the prototypical metal-free fullerene C_{60} [34,35].

3.2. Exciton dynamics of a K-doped $K_1(Sc_3N@C_{80})$ thin film

We now turn to the modification of the exciton dynamics of the $Sc_3N@C_{80}$ film after K doping and start with a K concentration with one K-atom per $Sc_3N@C_{80}$ molecule ($x = 1$). The corresponding time-resolved photoemission data are shown in Fig. 2.

First of all, K doping of the pristine $Sc_3N@C_{80}$ thin film results in a spectral broadening of the valence band structure coinciding with a work function decrease of $\Delta\Phi = 0.5 \pm 0.05$ eV [19]. This spectral broadening has its origin in the lifting of the degeneracy of the π -orbitals located at the C_{80} cage, which is caused by the reduced cage symmetry of the doped fullerene cage [19,44]. The most important change, however, is the population of the LUMO-derived state located at the Sc_3N core. It becomes occupied by the CT from the K atoms to the $Sc_3N@C_{80}$ molecules and leads to a new spectroscopic feature in the molecular valence band structure located 0.85 eV above E_{HOMO} [19,39]. It is marked by a black Gaussian curve underneath the photoemission spectra in Fig. 2(e).

Besides these spectral changes, K doping has a strong effect on the optically induced exciton dynamics of the $K_1(Sc_3N@C_{80})$ thin film which is reflected in the time-resolved photoemission data in Fig. 2. Time-resolved photoemission spectra of the excited state dynamics are shown as 2D plot in Fig. 2(a), the corresponding energy level diagram in Fig. 2(b). The first two steps of the exciton decay cascade are almost identical to the one of the pristine $Sc_3N@C_{80}$ film discussed above. Optical excitation with fs 3.2 eV laser pulses ($F = 0.55 \frac{mJ}{cm^2}$) results in the instantaneous formation of excitons 2.8 eV above E_{HOMO} (CT_2). Subsequently, these hot CT_2 excitons thermalize and continuously decay into the excitonic level CT_1 at lower energies. The exciton population of the CT_1 exciton persists only for a few hundreds of fs before vanishing from the excited states. In particular, we do not observe any indication for a long-lived trapping of excitons in the S_1 level as discussed beforehand for the pristine $Sc_3N@C_{80}$ films. The absence of the S_1 exciton in the excited states is the most severe difference between the exciton dynamics of the pristine and K-doped $Sc_3N@C_{80}$ thin films. The timescales of the exciton decay cascade can be determined by an independent spectral analysis of the time-dependent excited state spectra at each time delay using Gaussian curves at fixed excited state energies as discussed above. The best fitting results are shown in Fig. 2(c), the corresponding transient population of the CT_2 and the CT_1 excitons in Fig. 2(d). The best fitting result was obtained for an excited state energy of the CT_1 exciton that is slightly larger compared to the undoped $Sc_3N@C_{80}$ film. Importantly, no population could be detected for the energy position of the S_1 exciton (blue data points) confirming the absence of the S_1 exciton in this decay cascade. Using exponential decay functions, we observe depopulation times of $\tau_{CT_2,K} = 50 \pm 15$ fs and $\tau_{CT_1,K} = 0.5 \pm 0.2$ ps for the CT_2 and CT_1 excitons. The depopulation time for the CT_1 state is hence almost one order of magnitude smaller after K doping than in the pristine $Sc_3N@C_{80}$ film. These timescales can be directly compared to each other as the K doping study was conducted on the same sample as the study of the exciton dynamics

of the pristine $Sc_3N@C_{80}$ film. This suggests a new and significantly faster decay (or energy dissipation) mechanism for the thermalized CT_1 excitons due to the presence of K impurities.

These changes are also reflected in the transient linewidth broadening $\Delta FWHM$ of the valence states. EDCs at selected time delays are shown in Fig. 2(e), the extracted transient linewidth broadening of the HOMO is illustrated in Fig. 2(f). Similar to the pristine $Sc_3N@C_{80}$ film, we find an immediate broadening of the HOMO upon the excitation followed by a double-exponential decay back to the initial spectral linewidth. The decay times extracted from the double-exponential decay fit are $\tau_{TB2,K} = 75 \pm 35$ fs and $\tau_{TB1,K} = 0.4 \pm 0.2$ ps, respectively. Both decay times match the depopulation times of the CT_2 and CT_1 excitons in the excited states, demonstrating that both types of excitons still reveal dominant CT character, even after K doping.

Hence, K doping results in a significantly faster decay of the CT_1 excitons compared to the pristine $Sc_3N@C_{80}$ thin film. Crucially, these CT_1 excitons do not decay into lower lying excitonic levels, such as the S_1 exciton for the pristine film, but disappear completely from the excited state spectra. These observations could either be attributed to a direct recombination of the electron and hole of the CT_1 exciton, i.e., to a direct decay of the CT_1 exciton into the ground state, or to an efficient exciton dissociation and the generation of free carriers. In the following, we address this question by studying the exciton dynamics of K-doped $Sc_3N@C_{80}$ thin films for various K concentrations.

3.3. K concentration-dependent exciton dynamics of $K_x(Sc_3N@C_{80})$ thin films

The K concentration-dependent exciton dynamics of the $Sc_3N@C_{80}$ thin films can be determined from the photoemission data shown in Fig. 3. The K concentration of each doping step was identified by the characteristic line-shape of the (static) valence band structure [19] which is shown in Fig. 3(a) and (b) for selected K concentrations x . The continuous broadening of the valence band features with increasing K concentration can be attributed to a K-induced structural distortion of the C_{80} cage and a change in the cage symmetry. As pointed out earlier, both structural modifications result in a lifting of the energy degeneracy of the molecular valence orbitals [19,39,44]. In addition, increasing the K concentration leads to a gradual population of the LUMO-derived state at the Sc_3N core caused by a charge transfer from the K atoms into the $Sc_3N@C_{80}$ molecules. The amount of charge transfer can be estimated by the spectral weight of the corresponding LUMO-derived feature in the valence band spectra (black and gray Gaussian curve in Fig. 2(e) and Fig. 3(b), respectively). The charge transfer from K into the LUMO-derived state increases almost linearly with K concentration as illustrated in Fig. 3(c). This continuous population of the LUMO-derived state coincides also with a continuous reduction of the work function upon K doping. Both findings suggest a homogeneous distribution of K atoms within the molecular layer as well as in the near surface region of the molecular thin film.

For each doping step x , the excited states and the transient evolution of the valence states were studied by time-resolved photoemission. For clarity, we focus only on the transient linewidth broadening of the molecular valence bands, which is shown for the exemplary case of the HOMO level in Fig. 3(d) for selected K concentrations x . The temporal evolution of the linewidth broadening fully reflects the timescales of the population dynamics of the CT excitons within the molecular film. All transient linewidth traces exhibit the shape of a two-step decay process and were analyzed by the same double-exponential decay model discussed above. This analysis procedure yields two characteristic timescales $\tau_{TB2}(x)$ and $\tau_{TB1}(x)$ which reflect the depopulation times $\tau_{CT_2}(x)$ and $\tau_{CT_1}(x)$ of the CT excitons CT_2 and CT_1 , respectively.

Within our experimental uncertainty, the decay time $\tau_{TB2}(x)$ of the optically excited CT_2 excitons stays constant for all K concentrations. This suggests that the initial thermalization of the hot CT_2 excitons does not depend on the amount and density of the K atoms within

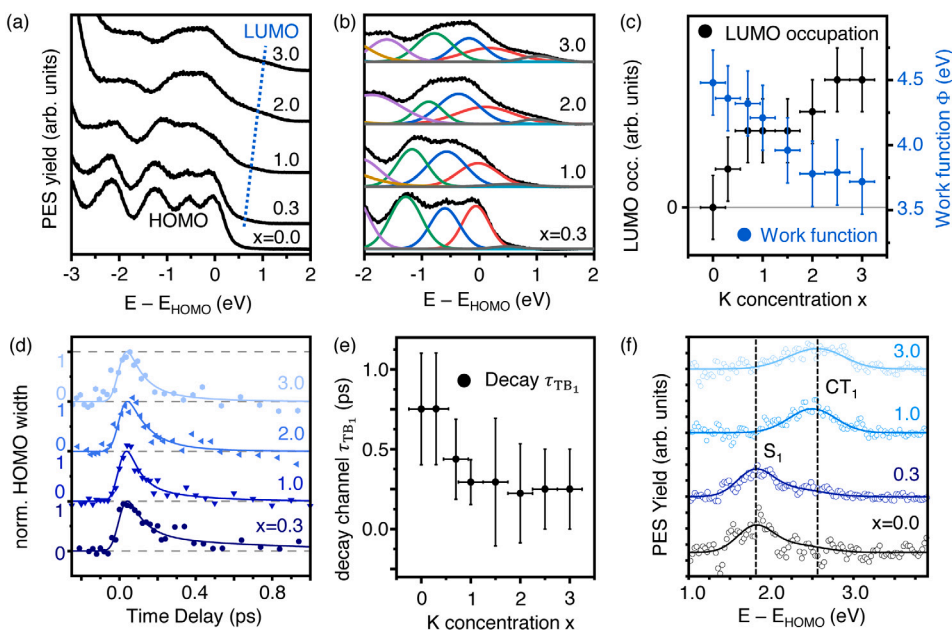


Fig. 3. K concentration-dependent exciton dynamics $K_x(\text{Sc}_3\text{N}@C_{80})$ multilayer film. (a) Valence band photoemission spectra of $K_x(\text{Sc}_3\text{N}@C_{80})$ for selected K doping concentrations x . The K concentrations x have been estimated by comparison of valence band photoemission spectra with literature [19]. The lineshape of the molecular valence band structure was analyzed by the fitting model shown in (b) underneath the experimental data. The Gaussian curves of different color indicate the spectral contributions of the HOMO-X levels, the gray one the contribution of the LUMO-derived state. The spectral weight (intensity) of the LUMO-derived state is shown in (c) together with the evolution of the work function of the molecular thin film depending on the K dopant concentration x . (d) Normalized transient HOMO linewidth (FWHM) for selected doping concentrations x . The transient broadening traces were shifted vertically for better comparability. The temporal evolution was modeled by a double-exponential decay function. (e) Decay times τ_{TB_1} for different dopant concentrations x . (f) Excited state spectra of $K_x(\text{Sc}_3\text{N}@C_{80})$ multilayer films for different K concentrations x recorded at a fixed time delay of $\Delta t = 300$ fs.

the $\text{Sc}_3\text{N}@C_{80}$ films. In contrast, we find characteristic changes of the depopulation time $\tau_{\text{CT}_1}(x) = \tau_{\text{TB}_1}(x)$ of the lower lying CT_1 exciton with increasing K concentration which are summarized in Fig. 3(e). Between $0.3 < x < 1$, the depopulation times $\tau_{\text{TB}_1}(x)$ decrease from 0.75 ± 0.25 ps to 0.25 ± 0.2 ps. For even larger K concentrations $x \geq 1$, $\tau_{\text{TB}_1}(x \geq 1)$ saturates at 0.25 ± 0.2 ps. This suggests a characteristic and qualitative modification of the exciton dynamics of the $K_x(\text{Sc}_3\text{N}@C_{80})$ films above the critical K concentration of $x = 1$.

Simultaneously, we also observe a characteristic change of the spectral yield of the S_1 exciton in the excited state energy range. This can be clearly observed in the time-resolved photoemission spectra in Fig. 3(f). These spectra were recorded at a time delay of 300 fs which revealed a clear spectral yield of the S_1 exciton for the pristine $\text{Sc}_3\text{N}@C_{80}$ film. From these data, we can deduce that the intensity of the S_1 signatures reduces upon K doping before vanishing completely for K concentrations $x \geq 1$.

Altogether, our findings point to a characteristic and qualitative modification of the exciton dynamics of the $K_x(\text{Sc}_3\text{N}@C_{80})$ films above the critical K concentration of $x = 1$. This is particularly interesting since a K doping concentration of one K atom per $\text{Sc}_3\text{N}@C_{80}$, is too small to lead to a complete filling of the LUMO state inside the carbon cage. This suggests that the population of the LUMO level is not the decisive factor in the qualitative modification of the exciton dynamics. Instead, we propose that the direct decay or dissociation of the CT_1 is most likely triggered by the spatial vicinity of the CT exciton and the K atom and not by a blocking effect of potential final states for the exciton relaxation process on the individual molecular sites.

4. Discussion

Our experimental findings have demonstrated the decisive influence of K doping for the exciton decay processes in thin films of endohedral metallofullerenes. First, optical excitation with visible light results in the formation of hot excitons with CT character (CT_2) which lead to a transient renormalization of the valence band structure of the

molecular thin films. These hot CT_2 excitons relax within sub-100 fs and transform into thermalized CT excitons (CT_1) with significantly longer depopulation times in the order of 1 ps. Finally, the CT excitons relax into a Frenkel-like excitonic level S_1 in which they become trapped for several ps. This exciton decay cascade is qualitatively identical to those of thin films of metal-free fullerenes [33–35,45,46]. Together with the energy positions of the excitonic levels, this observation suggests that the excitonic wave functions are mainly localized on the carbon cage of the $\text{Sc}_3\text{N}@C_{80}$ complexes.

After K doping, the exciton dynamics of the $\text{Sc}_3\text{N}@C_{80}$ thin films are strongly modified. For moderate K concentrations with less than one K atom per $\text{Sc}_3\text{N}@C_{80}$, we observe a continuous reduction of the depopulation times of the lowest lying CT exciton (CT_1) and a decreasing maximal population (maximum spectral weight) of the S_1 Frenkel exciton with increasing K concentration. For larger K concentrations with at least one K atom per $\text{Sc}_3\text{N}@C_{80}$ molecule, the CT_1 excitons no longer decay into the energetically lower S_1 state, but directly dissolve or dissociate with a constant depopulation time below 0.5 ps. This qualitative modification at the distinct K concentration of one K atom per $\text{Sc}_3\text{N}@C_{80}$ complex allows us to discuss several microscopic mechanisms that could explain the role of the K dopants for the exciton dynamics of the K-doped $\text{Sc}_3\text{N}@C_{80}$ thin films.

First of all, charge transfer into the $\text{Sc}_3\text{N}@C_{80}$ molecules results in an occupation of the 3d orbitals of the Sc atoms in the molecular core. As pointed out before, this additional occupation of the Sc_3N core derived states cannot influence the population of the S_1 exciton as the wavefunction of the S_1 exciton is mainly localized at the C_{80} cage. Instead, the charge transfer into the Sc_3N core could lead to a change of the cage symmetry of the pristine $\text{Sc}_3\text{N}@C_{80}$ [19,39] and a corresponding lattice distortions of the molecular films [44] upon K doping. As the excitons discussed in this work are localized at the C_{80} cage, both effects could in general influence the excited state decay channels for carbon-based clusterfullerenes [21]. However, these modifications of the structural and electronic properties of the molecules are not completed at a K concentration of one atom per $\text{Sc}_3\text{N}@C_{80}$

molecule, but still evolve even for larger K concentrations. This is clearly visible in our photoemission data in Fig. 3(a) which reveal continuous modifications of the molecular valence band structure for K concentrations $x \geq 1$.

Therefore, our findings indicate that the interaction between CT excitons and K-dopant atoms is most likely responsible for the qualitative modification in the exciton decay dynamics. The charge transfer process between the K atom and the $\text{Sc}_3\text{N@C}_{80}$ molecule leads to an (at least partial) ionic character of the K dopants in the molecular film. As a result, the dynamics of the CT excitons in the vicinity of a K ion are severely altered by the interaction of the microscopic charge distribution of the CT excitons and the Coulomb potential of the K ions. This additional interaction opens a new relaxation pathway that can severely alter the exciton decay cascade within the molecular film. It could either lead to a more efficient recombination of the electron and hole of the exciton or to a more preferred exciton dissociation.

An enhanced exciton decay via recombination is more likely in molecular materials with enhanced structural or charge order which, for instance, occurs by reducing the thermal motion of the molecules at lower temperatures [47,48]. This is clearly different in our case, where K doping results in a lattice distortions of the $\text{Sc}_3\text{N@C}_{80}$ molecule and an increase of K defect sites that break the translation symmetry of the molecular layer. Therefore, we propose that K doping significantly enhances the speed and efficiency of the exciton dissociation of CT excitons before becoming trapped in long-lived Frenkel-like excitonic states. Interestingly, CT excitons are often considered as precursors for the generation of free carriers in molecular materials at room temperature [33]. Therefore, it seems likely that the enhanced exciton dissociation efficiency upon K-doping also coincides with a highly efficient free charge carrier generation via CT exciton dissociation. Possibly, the ionic K dopants are able to capture the electron of the excitation via Coulomb attraction resulting in the generation of free holes in the $\text{Sc}_3\text{N@C}_{80}$ film.

Finally, we would like to point out that our model can also explain the changes of the depopulation time of the CT_1 exciton for low K doping concentrations. For low K concentrations, the probability to create CT excitons in direct vicinity of a K atom is rather low due to the random distribution of the K dopants in the molecular film and the stochastic process of the optical excitation. Hence, only a small number of CT excitons can dissociate via the ultrafast K-mediated relaxation channel while the other CT excitons decay with the intrinsic depopulation time of the pristine films before becoming trapped in the S_1 state. Our photoemission experiment spatially averages over all these processes and the recorded signal is composed of both decay cascades according to their relative contributions. With increasing K concentration, the relative contribution of the direct exciton dissociation process increases and the average depopulation time constant of CT_1 decreases until it saturates at $x = 1$. At this point, all CT excitons decay via the much faster relaxation channel mediated by the K intercalation-induced charge defects.

5. Conclusion

In conclusion, our investigation of the exciton dynamics in K-doped endohedral metallofullerenes has demonstrated the decisive role of alkali metal doping on the ultrafast exciton dynamics of molecular materials. We uncovered a K-induced ultrafast relaxation mechanism that prevents the trapping of excitons in long-lived excitonic states and results, most likely, in the generation of free charge carriers on ultrafast, sub-500 fs timescales. We therefore propose alkali metal doping of molecular films as a novel approach to enhance the light-to-charge carrier conversion efficiency in photovoltaic materials that could potentially pave the way towards the next generation of molecular-based light-harvesting applications with superior performance.

Declaration of competing interest

The authors declare that they have no known competing financial interests or personal relationships that could have appeared to influence the work reported in this paper.

Acknowledgments

The research leading to these results was financially supported by the Deutsche Forschungsgemeinschaft, Germany (DFG, SFB/TRR 88 “Cooperative Effects in Homo- and Heterometallic Complexes (3MET)” Project C9). Furthermore, S.E. acknowledge financial support from the Graduate School of Excellence Mainz, Germany (Excellence initiative DFG/GSC 266). This work is supported by the European Research Council (Grant 725767-hyControl).

References

- [1] G.K. Singh, Solar power generation by PV (photovoltaic) technology: A review, *Energy* 53 (2013) 1–13.
- [2] K. Yoshikawa, H. Kawasaki, W. Yoshida, T. Irie, E. Al, Silicon heterojunction solar cell with interdigitated back contacts for a photoconversion efficiency over 26%, *Nat. Energy* 2 (17032) (2017).
- [3] W.S. Yang, J.H. Noh, N.J. Jeon, Y.C. Kim, S. Ryu, J. Seo, S.I. Seok, High-performance photovoltaic perovskite layers fabricated through intramolecular exchange, *Science* 348 (6240) (2015) 1234–1237.
- [4] L. Meng, Y. Zhang, X. Wan, C. Li, X. Zhang, Y. Wang, X. Ke, Z. Xiao, L. Ding, R. Xia, H.L. Yip, Y. Cao, Y. Chen, Organic and solution-processed tandem solar cells with 17.3% efficiency, *Science* 361 (6407) (2018) 1094–1098.
- [5] J. Albero, P. Atienzar, A. Corma, H. Garcia, Efficiency records in Mesoscopic dye-sensitized solar cells, *Chem. Rev.* 15 (4) (2015) 803–828.
- [6] R.B. Ross, C.M. Cardona, F.B. Swain, D.M. Guldi, S.G. Sankaranarayanan, E. Van Keuren, B.C. Holloway, M. Drees, Tuning conversion efficiency in metallo endohedral fullerene-based organic photovoltaic devices, *Adv. Funct. Mater.* 19 (14) (2009) 2332–2337.
- [7] M. Schwarze, W. Tress, B. Beyer, F. Gao, R. Scholz, C. Poelking, K. Ortstein, A.A. Günther, D. Kasemann, D. Andrienko, K. Leo, Band structure engineering in organic semiconductors, *Science* 352 (6292) (2016) 1446–1450.
- [8] J.R. Pinzón, M.E. Plonska-Brzezinska, C.M. Cardona, A.J. Athans, S.S. Gayathri, D.M. Guldi, M.Á. Herranz, N. Martín, T. Torres, L. Echegoyen, $\text{Sc}_3\text{N@C}_{80}$ -ferrocene electron-donor/acceptor conjugates as promising materials for photovoltaic applications, *Angew. Chem., Int. Ed.* 47 (22) (2008) 4173–4176.
- [9] O. Ostroverkhova, Organic optoelectronic materials: Mechanisms and applications, *Chem. Rev.* 116 (22) (2016) 13279–13412.
- [10] C. Bizzarri, E. Spuling, D.M. Knoll, D. Volz, S. Bräse, Sustainable metal complexes for organic light-emitting diodes (OLEDs), *Coord. Chem. Rev.* 373 (2018) 49–82.
- [11] S. Krause, M.B. Casu, A. Schöll, E. Umbach, Determination of transport levels of organic semiconductors by UPS and IPS, *New J. Phys.* 10 (2008).
- [12] Q. Yang, M. Muntwiler, X.-Y. Zhu, Charge transfer excitons and image potential states on organic semiconductor surfaces, *Phys. Rev. B* 80 (11) (2009) 115214.
- [13] E.V. Tsiper, Z.G. Soos, W. Gao, A. Kahn, Electronic polarization at surfaces and thin films of organic molecular crystals: PTCDA, *Chem. Phys. Lett.* 360 (1–2) (2002) 47–52.
- [14] L. Bogner, Z. Yang, S. Baum, M. Corso, R. Fitzner, P. Bäuerle, K.J. Franke, J.I. Pascual, P. Tegeder, Electronic states and exciton dynamics in Dicyanovinyl-Sexithiophene on Au(111), *J. Phys. Chem. C* 120 (48) (2016) 27268–27275.
- [15] O. Ostroverkhova, D.G. Cooke, F.A. Hegmann, J.E. Anthony, V. Podzorov, M.E. Gershenson, O.D. Jurchescu, T.T.M. Palstra, Ultrafast carrier dynamics in pentacene, functionalized pentacene, tetracene and rubrene single crystals, *Appl. Phys. Lett.* 88 (16) (2006) 162101.
- [16] I. Salzmann, G. Heimel, S. Duhm, M. Oehzelt, P. Pingel, B.M. George, A. Schnegg, K. Lips, R.-P. Blum, A. Vollmer, N. Koch, Intermolecular hybridization governs molecular electrical doping, *Phys. Rev. Lett.* 108 (3) (2012) 035502.
- [17] N. Haag, D. Lüftner, F. Haag, J. Seidel, L.L. Kelly, G. Zamborlini, M. Jugovac, V. Feyrer, M. Aeschlimann, P. Puschnig, M. Cinchetti, B. Stadtmüller, Signatures of an atomic crystal in the band structure of a C_{60} thin film, *Phys. Rev. B* 101 (16) (2020).
- [18] F. Bussolotti, J. Yang, T. Yamaguchi, K. Yonezawa, K. Sato, M. Matsunami, K. Tanaka, Y. Nakayama, H. Ishii, N. Ueno, S. Kera, Hole-phonon coupling effect on the band dispersion of organic molecular semiconductors, *Nature Commun.* 8 (1) (2017) 173.
- [19] L. Alvarez, T. Pichler, T. Pichler, P. Georgi, T. Schwieger, H. Peisert, L. Dunsch, Z. Hu, M. Knupfer, J. Fink, P. Bressler, M. Mast, M.S. Golden, Electronic structure of pristine and intercalated $\text{Sc}_3\text{N@C}_{80}$ metallofullerene, *Phys. Rev. B* 66 (3) (2002) 351071–351077.

- [20] S. Sato, S. Seki, G. Luo, M. Suzuki, J. Lu, S. Nagase, T. Akasaka, Tunable charge-transport properties of I h-C 80 endohedral metallofullerenes: Investigation of $\text{La}_2@C_{80}$, $\text{Sc}_3\text{N}@C_{80}$ and $\text{Sc}_3\text{C}_2@C_{80}$, *J. Am. Chem. Soc.* 134 (28) (2012) 11681–11686.
- [21] B. Wu, J. Hu, P. Cui, L. Jiang, Z. Chen, Q. Zhang, C. Wang, Y. Luo, Visible-light photoexcited electron dynamics of Scandium endohedral metallofullerenes: The cage symmetry and substituent effects, *J. Am. Chem. Soc.* 137 (27) (2015) 8769–8774.
- [22] A. Mateo-Alonso, D.M. Guldi, F. Paolucci, M. Prato, Fullerenes: multitask components in molecular machinery, *Angew. Chem., Int. Ed.* 46 (43) (2007) 8120–8126.
- [23] H.W. Kroto, J.R. Heath, S.C. O'Brien, R.F. Curl, R.E. Smalley, C_{60} : Buckminsterfullerene, *Nature* 318 (6042) (1985) 162–163.
- [24] S. Stevenson, G. Rice, T. Glass, K. Harich, F. Cromer, M.R. Jordan, J. Craft, E. Hadju, R. Bible, M.M. Olmstead, K. Maitra, A.J. Fisher, A.L. Balch, H.C. Dorn, Small-bandgap endohedral metallofullerenes in high yield and purity, *Nature* 401 (6748) (1999) 55–57.
- [25] A. Popov, S. Yang, L. Dunsch, Endohedral fullerenes, *Chem. Rev.* 113 (2013) 5989–6113.
- [26] D.S. Bethune, R.D. Johnson, J.R. Salem, M.S. de Vries, C.S. Yannoni, Atoms in carbon cages: The structure and properties of endohedral fullerenes, *Nature* 366 (6451) (1993) 123–128.
- [27] C.J. Bardeen, The structure and dynamics of molecular excitons, *Annu. Rev. Phys. Chem.* 65 (1) (2014) 127–148.
- [28] P. Cudazzo, M. Gatti, A. Rubio, F. Sottile, Frenkel versus charge-transfer exciton dispersion in molecular crystals, *Phys. Rev. B* 88 (19) (2013) 558.
- [29] K. Harigaya, S. Abe, Exciton and lattice-fluctuation effects in optical spectra of C_{60} , *Mol. Cryst. Liq. Cryst. Sci. Technol. Sect. A. Mol. Cryst. Liq. Cryst.* 256 (256) (1994) 825–830.
- [30] M. Panhans, S. Hutsch, J. Benduhn, K.S. Schellhammer, V.C. Nikolis, T. Vangerven, K. Vandewal, F. Ortmann, Molecular vibrations reduce the maximum achievable photovoltage in organic solar cells, *Nature Commun.* 11 (1) (2020) 1488.
- [31] T. Rangel, A. Rinn, S. Sharifzadeh, F.H. da Jornada, A. Pick, S.G. Louie, G. Witte, L. Kronik, J.B. Neaton, S. Chatterjee, Low-lying excited states in crystalline perylene, *Proc. Natl. Acad. Sci. USA* 115 (2) (2018) 284–289.
- [32] X.-Y. Zhu, Q. Yang, M. Muntwiler, Charge-transfer excitons at organic semiconductor surfaces and interfaces, *Acc. Chem. Res.* 42 (11) (2009) 1779–1787.
- [33] M. Causa, I. Ramirez, J.F. Martinez Hardigree, M. Riede, N. Banerji, Femtosecond dynamics of photoexcited C_{60} films, *J. Phys. Chem. Lett.* 9 (8) (2018) 1885–1892.
- [34] B. Stadtmüller, S. Emmerich, D. Jungkenn, N. Haag, M. Rollinger, S. Eich, M. Maniraj, M. Aeschlimann, M. Cinchetti, S. Mathias, Strong modification of the transport level alignment in organic materials after optical excitation, *Nature Commun.* 10 (1) (2019) 1–9.
- [35] S. Emmerich, S. Hedwig, B. Arnoldi, J. Stöckl, F. Haag, R. Hemm, M. Cinchetti, S. Mathias, B. Stadtmüller, M. Aeschlimann, Ultrafast charge-transfer exciton dynamics in C_{60} thin films, *J. Phys. Chem. C* 124 (43) (2020) 23579–23587.
- [36] T. Fujita, S. Atahan-Evrenk, N.P.D. Sawaya, A. Aspuru-Guzik, Coherent dynamics of mixed Frenkel and charge-transfer excitons in Dinaphtho2, 3-b:2'3'-fthieno3, 2-b-thiophene thin films: The importance of hole delocalization, *J. Phys. Chem. Lett.* 7 (7) (2016) 1374–1380.
- [37] H. Tamura, I. Burghardt, Ultrafast charge separation in organic photovoltaics enhanced by charge delocalization and vibronically hot exciton dissociation, *J. Am. Chem. Soc.* 135 (44) (2013) 16364–16367.
- [38] E. Varene, L. Bogner, C. Bronner, P. Tegeder, Ultrafast exciton population, relaxation and decay dynamics in thin oligothiophene films, *Phys. Rev. Lett.* 109 (20) (2012) 207601.
- [39] A.A. Popov, L. Dunsch, Hindered cluster rotation and ^{45}Sc hyperfine splitting constant in distonoid anion radical $\text{Sc}_3\text{N}@C_{80}^-$, and spatial spin - charge separation as a general principle for anions of endohedral fullerenes with metal-localized lowest unoccupied molecular orbitals, *J. Am. Chem. Soc.* 130 (52) (2008) 17726–17742.
- [40] J. Seidel, L.L. Kelly, M. Franke, G. Van Straaten, C. Kumpf, M. Cinchetti, M. Aeschlimann, B. Stadtmüller, Adsorption-induced pyramidal distortion of the trimetallic nitride core inside the endohedral fullerene $\text{Sc}_3\text{N}@C_{80}$ on the Ag(111) surface, *Phys. Rev. B* 98 (8) (2018) 1–10.
- [41] S. Eich, A. Stange, A. Carr, J. Urbancic, T. Popmintchev, M. Wiesenmayer, K. Jansen, A. Ruffing, S. Jakobs, T. Rohwer, S. Hellmann, C. Chen, P. Matyba, L. Kipp, K. Rossnagel, M. Bauer, M. Murnane, H. Kapteyn, S. Mathias, M. Aeschlimann, Time- and angle-resolved photoemission spectroscopy with optimized high-harmonic pulses using frequency-doubled Ti:Sapphire lasers, *J. Electron Spectrosc.* 195 (2014) 231.
- [42] T. Popmintchev, M.-C. Chen, P. Arpin, M.M. Murnane, H.C. Kapteyn, The attosecond nonlinear optics of bright coherent X-ray generation, *Nat. Photonics* 4 (12) (2010) 822–832.
- [43] R.R. Zope, S. Bhusal, L. Basurto, T. Baruah, K. Jackson, Site specific atomic polarizabilities in endohedral fullerenes and carbon anions, *J. Chem. Phys.* 143 (8) (2015) 084306.
- [44] K. Harigaya, Lattice distortion and energy-level structures in doped C_{60} and C_{70} molecules studied with the extended Su-Schrieffer-Heeger model: Polaron excitations and optical absorption, *Phys. Rev. B* 45 (23) (1992) 13676–13684.
- [45] R. Jacquemin, S. Kraus, W. Eberhardt, Direct observation of the dynamics of excited electronic states in solids: fs time-resolved photoemission of C_{60} , *Solid State Commun.* 105 (7) (1998) 449–453.
- [46] A.C. Rosenfeldt, B. Göhler, H. Zacharias, Time-resolved photoelectron spectroscopy of low-energy excitations of $4\times 4 C_{60}/\text{Cu}(111)$, *J. Chem. Phys.* 133 (23) (2010).
- [47] M.S. Dresselhaus, G. Dresselhaus, A.M. Rao, P.C. Eklund, Optical properties of C_{60} and related materials, *Synth. Met.* 78 (3) (1996) 313–325.
- [48] A.-M. Janner, R. Eder, B. Koopmans, H.T. Jonkman, G.A. Sawatzky, Excitons in C_{60} studied by temperature-dependent optical second-harmonic generation, *Phys. Rev. B* 52 (24) (1995) 158–164.